Effect of aspect ratio and eccentricity on heat transfer from a cylinder in a cavity

Syeda Humaira Tasnim
Department of Industrial and Production Engineering, Shahjalal University of Science and Technology, Bangladesh

Shohel Mahmud and Prodip Kumar Das
Department of Mechanical Engineering, Bangladesh University of Engineering and Technology (BUET), Bangladesh

Received January 2002
Accepted May 2002

Keywords *Flow, Finite volume, Heat transfer, Natural convection*

Abstract *This paper presents the hydrodynamic and thermal behavior of fluid that surrounds an isothermal circular cylinder in a square cavity. Simulations were carried out for four aspect ratios (defined by* L/D*), i.e. 2.0, 3.0, 4.0, 5.0. An incompressible flow of Newtonian fluid is considered. Prandtl number is assumed constant and equal to 1. Effect of eccentric positions ($\varepsilon = -0.5$ and 0.5) of the cylinder with respect to the cavity was carried out at* $L/D = 2.0$*. Predicted results for eccentric cases are compared with concentric ($\varepsilon = 0.0$) case. Grashof number is based on the diameter of the cylinder and ranges from 10 to 10^6. The control volume based finite volume method is used to discretize the governing equations in cylindrical coordinate. SIMPLE algorithm is used. A collocated variable arrangement is considered and SIP solver is employed to solve the system of equations. Parametric results are presented in the form of streamlines and isothermal lines for both eccentric and concentric positions. Heat transfer distribution along the perimeter of the cylinder is presented in the form of local Nusselt number. Predicted results show good agreement with the results described by Cesini* et al. *(1999).*

Nomenclature

A = coefficient matrix
C_p = specific heat
D = diameter of the cylinder
g = gravity acceleration
Gr = Grashof number
h = heat transfer coefficient
k = thermal conductivity of fluid
L = length & width of walls
Nu = Nusselt number
n = surface normal
Pr = Prandtl number
r = radial coordinate
R = dimensionless radial coordinate
P = pressure
P^* = modified pressure
T = temperature
u = radial velocity component
v = tangential velocity component
U_r = dimensionless radial velocity
U_θ = dimensionless tangential velocity

Greek symbols

α = thermal diffusivity
β = thermal expansion coefficient
ε = eccentricity (see equation (16))
ϑ = any variable

International Journal of Numerical Methods for Heat & Fluid Flow, Vol. 12 No. 7, 2002, pp. 855-869.

DOI 10.1108/09615530210443061

Φ = total mass flux
Ω = convective or diffusive flux
μ = dynamic viscosity of fluid
ρ = density of fluid
ψ = stream function
σ = an index
θ = tangential coordinate
Θ = dimensionless temperature

Subscripts/superscripts
av = average value
D = based on diameter
C = at cylinder wall
L = local value
ref = reference value
w = at cavity wall
∞ = ambient condition

1. Introduction

Heat transfer from circular cylinder in a cavity has many engineering applications like industrial heat exchanger, evaporator and condenser unit, cooling system of machine parts, electronic packages, etc. Numerous literatures are available for the concentric cylinder in a rectangular cavity at different boundary conditions. Eccentric cases are also important and have not been studied to a great extent. Natural convection from single horizontal circular cylinder (Cesini *et al.*, 1999; Farouk and Guceri, 1981) and from square cylinder (Tasnim and Mahmud, 1999) in an enclosed space has been investigated in the past. Some numerical and experimental investigations are available (Prusa and Yao, 1983; Kuhen and Goldstein, 1976; 1978) that considered heat transfer inside concentric and eccentric cylindrical annular space. In the present paper, heat transfer from a horizontal circular cylinder placed inside a square enclosure with two isothermal vertical walls and two adiabatic horizontal walls is investigated numerically. Cylindrical surface is taken as isothermal. The objective of the present investigation is to observe the heat transfer performance around a cylinder at two eccentric (one positive and one negative) positions and concentric position at different Grashof numbers and aspect ratio (L/D). Only the effect of vertical eccentricity is considered in the present investigation.

2. Mathematical modeling

In the present investigation, we used the conservation equations (continuity, momentum and energy) in cylindrical coordinates of the following form:

$$\frac{\partial U_\theta}{\partial R} + \frac{1}{R}\frac{\partial U_r}{\partial \theta} + \frac{U_\theta}{R} = 0 \tag{1}$$

$$U_r\frac{\partial U_r}{\partial R} + \frac{U_\theta}{R}\frac{\partial U_r}{\partial \theta} = -\frac{1}{R}\frac{\partial P^*}{\partial \theta} - \frac{U_r U_\theta}{R} + \Pr\left(\frac{\partial^2 U_r}{\partial R^2} + \frac{1}{R}\frac{\partial U_r}{\partial R} + \frac{1}{R^2}\frac{\partial^2 U_r}{\partial \theta^2} - \frac{U_r}{R^2} + \frac{2\partial U_\theta}{R^2 \partial \theta}\right) - \Pr\ Ra\Theta\ \mathrm{Sin}\,\theta \tag{2}$$

$$U_r\frac{\partial U_\theta}{\partial R}+\frac{U_\theta}{R}\frac{\partial U_\theta}{\partial\theta}=-\frac{\partial P^*}{\partial R}-\frac{U_r^2}{R}+\Pr\left(\frac{\partial^2 U_\theta}{\partial R^2}+\frac{1}{R}\frac{\partial U_\theta}{\partial R}+\frac{1}{R^2}\frac{\partial^2 U_\theta}{\partial\theta^2}-\frac{U_\theta}{R^2}+\frac{2\partial U_r}{R^2\partial\theta}\right)+\Pr\ Ra\Theta\ \mathrm{Cos}\,\theta \tag{3}$$

By introducing the following dimensionless variables:

$$R=\frac{r}{D/2},\quad \Theta=\frac{T-T_W}{T_C-T_W},\quad U_r=\frac{D\rho\Pr}{2\mu}u,\quad U_\theta=\frac{D\rho\Pr}{2\mu}v \tag{4a}$$

$$Ra=\frac{(D/2)^3\beta g(T_W-T_C)}{\nu\alpha},\quad [\mathrm{Nu}_D]_L=\frac{hD}{k_f},\quad [\mathrm{Nu}_D]_{av}=\frac{1}{\pi D}\int_0^{2\pi}[\mathrm{Nu}_D]_L\,\mathrm{d}\theta \tag{4b}$$

$$P^*=\frac{\rho(r\Pr)^2}{\mu^2}\left[P+\left\{\rho_{ref}(1-\beta T_{ref})-\frac{\Pr^2\rho^3\beta T_{ref}}{\mu}\right\}gr\cos\theta\right] \tag{4c}$$

Neglecting compression work and viscous dissipation, the energy equation reduces to:

$$U_r\frac{\partial\Theta}{\partial R}+\frac{U_\theta}{R}\frac{\partial\Theta}{\partial\theta}=\frac{\partial^2\Theta}{\partial R^2}+\frac{1}{R}\frac{\partial\Theta}{\partial R}+\frac{1}{R^2}\frac{\partial^2\Theta}{R^2\partial\theta^2} \tag{5}$$

$$\varrho=\varrho_{ref}\left[1-\beta(T-T_{ref})\right] \tag{6}$$

Above equations are discretized using control volume based finite volume method with collocated variable arrangement. The transport equations are integrated over a finite number of control volumes, leading to a balance equation of fluxes (Φ) through the control volume (CV) faces, and volumetric sources S (here pressure and bouncy forces). Figure 1(a) and (b) shows the grid structure with computational domain. The computational domain of integration is divided into nonuniform control volumes, where more grids are adopted near the cylinder surface. Figure 2 shows an individual CV of the domain. The balance flux equation can be written in the following form:

$$\Phi_e-\Phi_w+\Phi_n-\Phi_s=S \tag{7}$$

Mass fluxes through the west face 'w' and the south face 's' (see Figure 2) are calculated using the following equations:

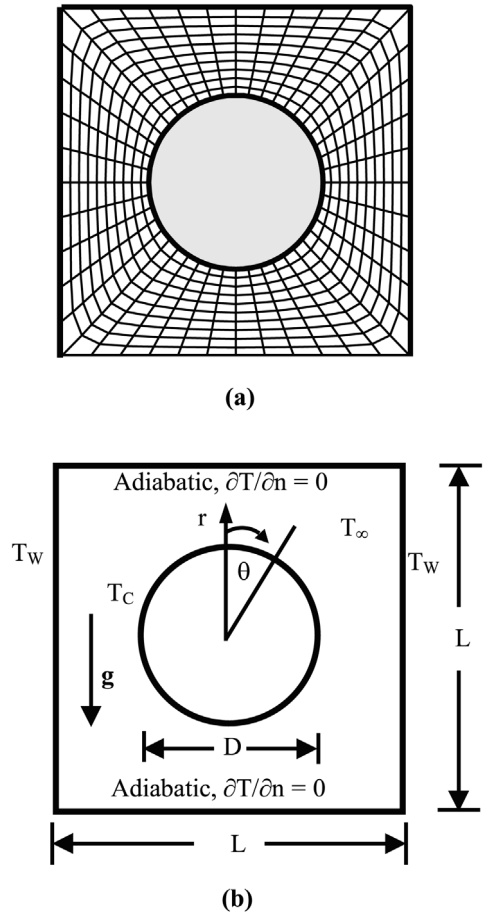

Figure 1.
(a) Numerical grid structure and (b) computational domain

$$\dot{m}_w = (\rho U_r r \delta\theta)_{\mathrm{w}} \tag{8}$$

$$\dot{m}_s = (\rho U_\theta \delta r)_{\mathrm{s}} \tag{9}$$

where U_r and U_θ are the radial and tangential velocity components and are considered to represent the mean values over the CV face. These values are calculated using an appropriate interpolation formula defined by Ferziger and Peric (1996). Then the convective flux of a variable φ is evaluated as

$$\Omega_{\mathrm{w}}^{\mathrm{C}} = \dot{m}\varphi_{\mathrm{w}} \tag{10}$$

where φ_{w} stands for the mean value of the transported variables (U_r, U_θ or T) at the CV face 'w'. The estimate for this value is expressed in terms of the nodal values by employing the central difference scheme (CDS), which implies linear

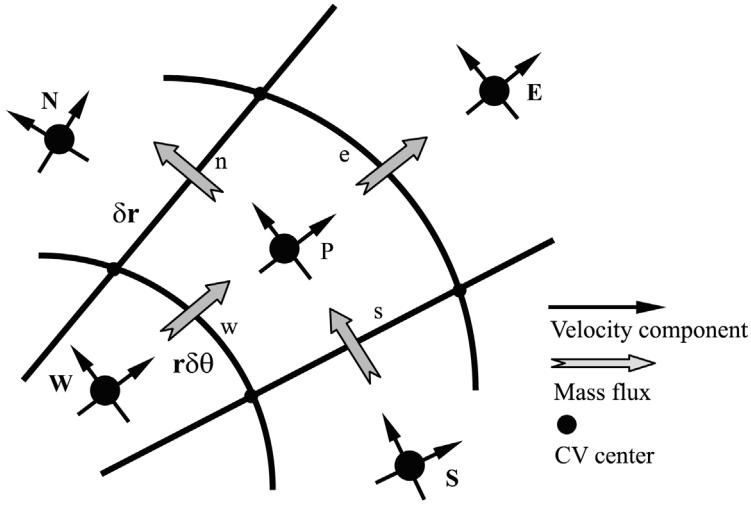

Figure 2.
A typical CV showing different parameters

interpolation (Ferziger and Peric, 1996) between nodes W and P. The diffusive flux is estimated using the CDS scheme and can be written in the following form:

$$\Omega_{\mathrm{w}}^{D} = -\left(\frac{\mu}{\mathrm{Pr}}\right)\frac{\varphi_{\mathrm{p}} - \varphi_{\mathrm{w}}}{r_{\mathrm{p}} - r_{\mathrm{w}}} r\delta\theta \tag{11}$$

The source terms are integrated over the cell volume. This is done by evaluating the specific source at the central point P, which is then taken to represent the mean value over the whole CV – hence the integration involves only multiplication of the nodal value by the cell volume. The source of the radial momentum then becomes:

$$S = r\delta\theta(P_{\mathrm{e}} - P_{\mathrm{w}}) + \rho_0 \beta g_r (T_{\mathrm{p}} - T_0) r\delta\theta\delta r \tag{12}$$

Finally equation (7) can be written in the following form

$$A_{\mathrm{P}}\varphi_{\mathrm{P}} + \sum_{m} A_m \varphi_m = S_\varphi \tag{13}$$

where $m = \mathrm{E}, \mathrm{W}, \mathrm{N}, \mathrm{S}$ are the four immediate neighbors of point P, and φ stands for U_r, U_θ or T.

SIMPLE algorithm (Patankar, 1980) is used for the solution of coupled velocity, temperature, and pressure equations. Solution starts with a guessed pressure field. In each iteration, value of pressure, mass flux and other variables are taken from previous iteration and using these values momentum equations are assembled. This is solved by one inner iteration of SIP algorithm (Ferziger and Peric, 1996). Calculated velocity field is used to determine new

mass fluxes. Pressure correction equation is then solved. After pressure and velocity correction, temperature equation is assembled and solved. Solution procedures with detailed algorithm are available (Patankar, 1980; Ferziger and Peric, 1996). The convergence criterion used here is that the sum of absolute residuals in all equations is reduced by at least six orders of magnitude. For further stabilization of numerical solution, underrelaxation factors of 0.7, 0.7, 0.2 and 0.9 are used for velocities, pressure, and temperature equations. For the present problem, boundary conditions are:

$$\text{At cylinder wall}: R = 1, \quad U_r = U_\theta = 0 \text{ and } \Theta = 1 \tag{14}$$

The boundary conditions for square cavity wall is as follows:

$$\text{At } R = \left[\frac{L/D}{2\cos\left[\theta - \frac{\pi}{4}\sigma\right]}\right]_{\sigma=0,2,4,6} + \left[\frac{L/D}{2\cos\left[\frac{\pi}{4}(\sigma+1) - \theta\right]}\right]_{\sigma=1,3,5,7} \tag{15}$$

$U_r = U_\theta = 0.0$, $\Theta = 0.0$ at $\sigma = 1, 2, 5, 6$ and $\partial\Theta/\partial n = 0.0$ at $\sigma = 0, 3, 4, 7$ where $\sigma = \text{Int}[4\theta/\pi]$.

3. Results and discussions

Numerical grid structure and computational domain with different geometrical variables and boundary conditions used in present investigation are shown in Figure 1(a) and (b). The diameter of the cylinder is D and width and height of the square enclosure is L. The cylinder surface is isothermal with temperature T_C. Two vertical walls of the enclosure are also isothermal with temperature T_W. The initial fluid temperature is T_∞. The top and bottom horizontal walls are considered adiabatic. Four grid sizes are chosen to carry out present simulation. In Figure 3(a), local Nusselt number distribution is presented for $\text{Gr} = 10^4$ for four prescribed grid sizes. Except for the coarse grid (20×10) solution, the $[\text{Nu}_D]_L - \theta$ profiles for the remaining three grid sizes (e.g. 40×20, 80×40, and 160×80) coincide with each other. Throughout this paper, results of 80×40 grid are presented. Predicted data from the present study is compared with the work of Cesini *et al.* (1999) in Figure 3(b). Cesini *et al.* (1999) finite element method is based on the streamfunction–vorticity formulation of the momentum equation. For both cases (present prediction and results from Cesini *et al.* (1999)) Prandtl number of the fluid is 1.0. This comparison shows excellent agreement.

3.1 Effect of aspect ratio

The geometric parameter, aspect ratio, is defined by L/D. Simulation was carried out for four different L/D ratios (2.0, 3.0, 4.0 and 5.0). Figure 4(a) and (b) shows the variation of local Nusselt number (based on the diameter) along the perimeter of the cylinder for two selected Grashof numbers 10^2 and 10^4.

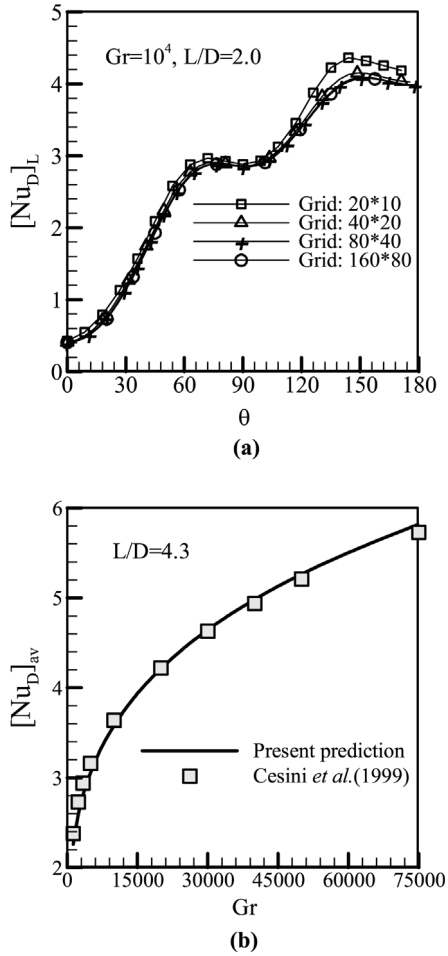

Figure 3.
(a) Grid sensitivity test and (b) code verification test

Figure 5 shows the variation of global value of Nusselt number as a function of Grashof number. Average heat transfer shows the linear variation with Grashof number in log-log plot. A critical range of Grashof number (2×10^3-3×10^3) is numerically determined. Below this range, lower L/D shows higher heat transfer rate and above this range the reverse scenario occurred. Below the critical range, viscous force is high and heat transfer is mainly dominated by conduction from one layer of fluid to another. In lower L/D, space between cylinder and cavity wall is small thus showing higher heat transfer rate. Buoyancy force dominates over viscous force after upper critical range. Convective currents are retarded due to narrow space at lower L/D compared to the higher values of L/D. So, average heat transfer falls here for lower L/D ratio.

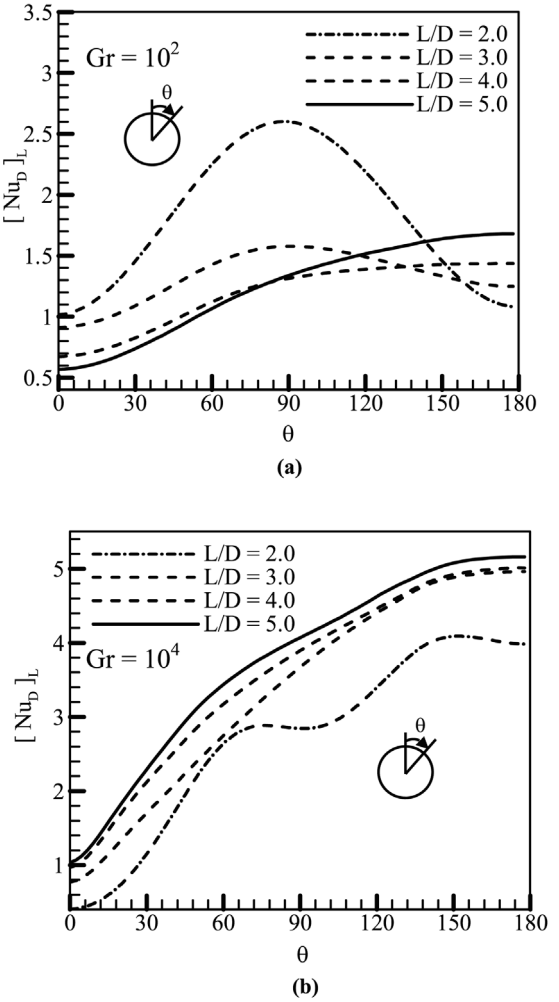

Figure 4.
Nusselt number distribution along the perimeter at (a) $Gr = 10^2$ and (b) $Gr = 10^4$

3.2 Effect of eccentricity

Effect of eccentricity at four different Grashof numbers on local heat transfer is shown in Figure 6(a)-(d). At a very small value of Grashof number (10^1), viscous force dominates and the heat transfer around the cylinder is similar to the conduction. At $\varepsilon = 0.0$, distribution pattern is symmetrical about the point located at 90° angular position. At positive eccentricity $\varepsilon = 0.5$, the gap between the cylinder and the upper adiabatic wall is smaller compared to the gap between the cylinder and the lower adiabatic wall. At the upper side, temperature gradient normal to the cylinder surface is comparatively higher than the lower surface, showing higher heat transfer rate before the point

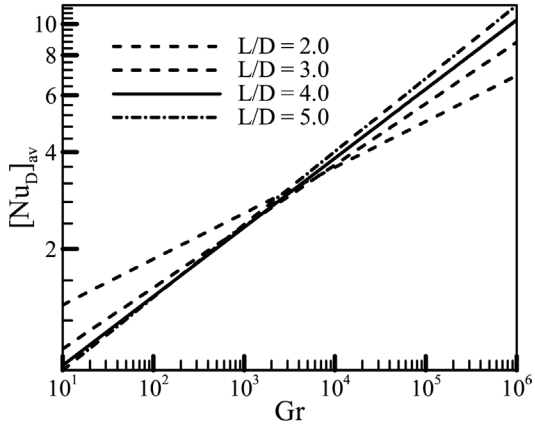

Figure 5.
Average Nusselt number as a function of Grashof number

located at 90°. However, this scenario reverses at negative eccentricity $\varepsilon = -0.5$. At high Grashof number, buoyancy force starts to dominate both the flow and thermal fields. As $T_C > T_W$, fluid inside the enclosure rises upward along the cylindrical surface and reaches the top adiabatic wall and is deflected away

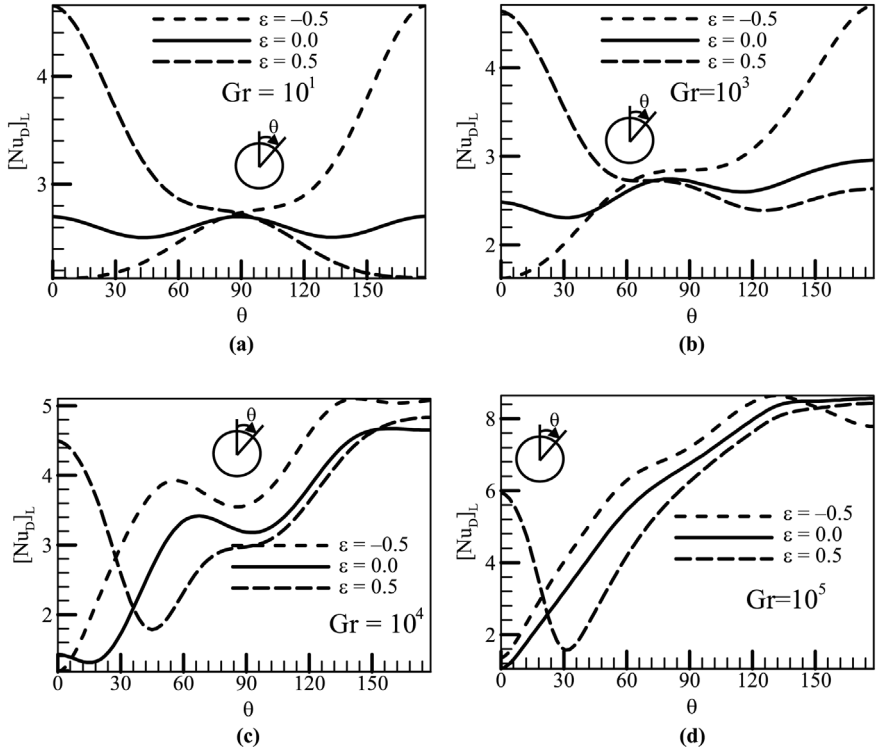

Figure 6.
Local Nusselt number distribution at different eccentricity for $L/D = 2.0$

from the cylinder. Upward velocity of flow increases with the increase of Grashof number. Temperature gradient in such cases is higher at the bottom of the cylinder, showing higher heat transfer rate. Positive eccentricity still shows a higher rate of heat transfer at the 0° position due to smaller gap between cylinder and top adiabatic surface then starts to fall to a minimum point and again rises.

3.3 Flow and thermal fields

Flow and thermal fields are presented in the form of constant streamlines and isothermal lines for different eccentricity in Figures 7-9. For convenience of presentation, both streamlines and isothermal lines are plotted opposite to each other about the symmetrical axis on the same figure. The following subsections will give a brief idea of flow and thermal fields at different eccentric position of cylinder.

(a) *Negative eccentricity*, $\varepsilon = -0.5$. Eccentricity is measured from the center of the enclosure vertically upward (positive) or vertically downward (negative). If O is the center of the enclosure and $\bar{\mathrm{O}}$ is the new position of the center of the cylinder vertically upward or downward, then eccentricity is defined as

$$\varepsilon = \frac{L - D}{R}\left(\frac{\mathrm{O}\bar{\mathrm{O}}}{D}\right) \tag{16}$$

where R is the radius of the cylinder. Figure 7 shows the flow and thermal field for negative eccentricity. At $\mathrm{Gr} = 10^1$, high viscous force produces a very weak circulation with almost negligible velocity components. Isothermal lines show the characteristics of conduction. Near the bottom wall, temperature gradient normal to the cylindrical surface is higher and decreases gradually along the perimeter. This bottom part of the cylinder shows higher value of heat transfer as shown in Figure 6(a). At $\mathrm{Gr} = 10^4$, circulatory vortex has higher strength at the upper part of the cylinder making thermal boundary layer. At $\mathrm{Gr} = 10^5$, temperature contour swirls due to high convective current.

(b) *Zero eccentricity*, $\varepsilon = 0.0$. This is the case of concentric cylinder in a cavity. Flow and thermal fields are presented in Figure 8(a)-(c). Two recirculation zones are clearly shown beside the cylinder, growing in intensity with increasing Grashof numbers. The temperature distribution on the upper part of the cavity is characteristic of natural convection from circular objects. With the increase of Grashof number, buoyancy force starts to dominate the flow field. Upward flow velocity increases shifting the core of the circulatory zone upward. At $\mathrm{Gr} = 10^5$, intensity of circulation is higher at the upper portion of the enclosure showing only one kidney-shaped core. It is clear from the Figure 8(c) that temperature gradient increases along the perimeter of the cylinder (θ increasing) thus showing higher heat transfer rate (Figure 6 (d)).

(c) *Positive eccentricity*, $\varepsilon = 0.5$. Flow and thermal fields for positive eccentricity are shown in Figure 9(a)-(c). At $\mathrm{Gr} = 10^1$, circulation zone shows

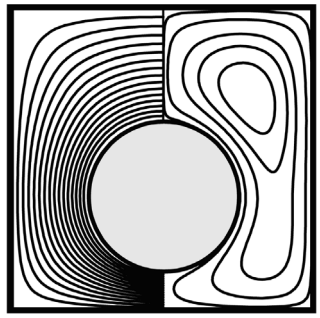

(a) Gr = 10

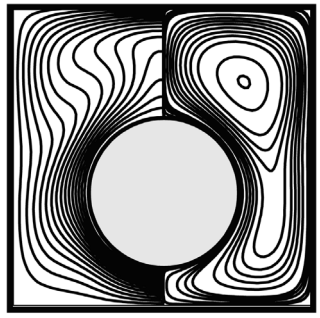

(b) Gr = 10^4

(c) Gr = 10^5

Figure 7.
Isothermal lines and streamlines for $\varepsilon = -0.5$ and (a) Gr = 10, (b) Gr = 10^4, and (c) Gr = 10^5

just opposite nature of negative eccentricity. Temperature gradient is higher at the upper portion of the cylinder showing higher heat transfer rate. At Gr = 10^4, core of the circulatory vortex starts to divide into two distinct parts. But at Gr = 10^5, circulatory zone shows only one core and isothermal lines give clear indication of the formation of thermal boundary layer. A dead zone is observed at the uppermost portion of the cylinder due to the small gap between cylinder

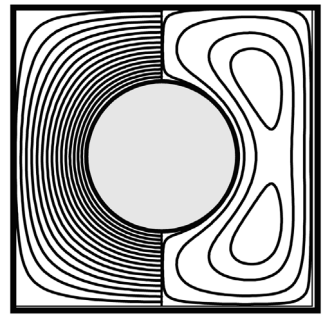

(a) Gr = 10

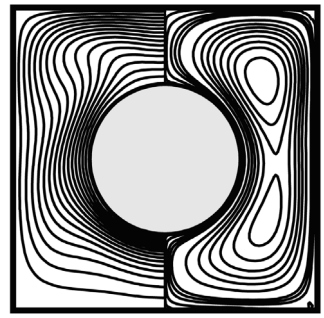

(b) Gr = 10^4

(c) Gr = 10^5

Figure 8.
Isothermal lines and streamlines for $\varepsilon = 0.0$ and (a) Gr = 10, (b) Gr = 10^4, and (c) Gr = 10^5

surface and enclosure wall. This dead zone is responsible for initial falling tendency of heat transfer shown in Figure 6(d).

Average heat transfer

Average heat transfer is presented in terms of average Nusselt number in Figure 10 as a function of Grashof number at three different eccentricities. Concentric case ($\varepsilon = 0.0$) shows lower value of average heat transfer compared

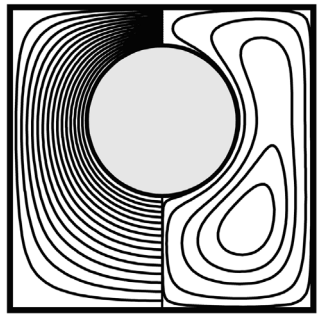

(a) Gr = 10

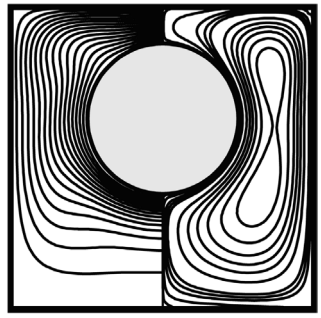

(b) G r = 10^4

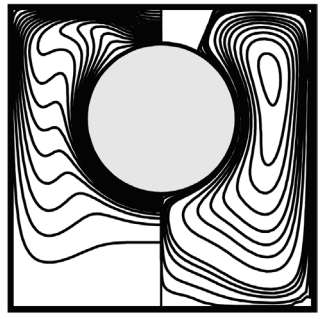

(c) Gr = 10^5

Figure 9.
Isothermal lines and streamlines for $\varepsilon = 0.5$ and (a) Gr = 10, (b) Gr = 10^4, and (c) Gr = 10^5

to the same at positive and negative eccentricity. For the range Gr = 10^1-10^6, the average heat transfer rate is higher at positive eccentricity for $L/D = 2.0$.

Conclusions

Heat transfer around a circular cylinder at two different eccentric positions and concentric position in a square enclosure is studied for a particular aspect ratio

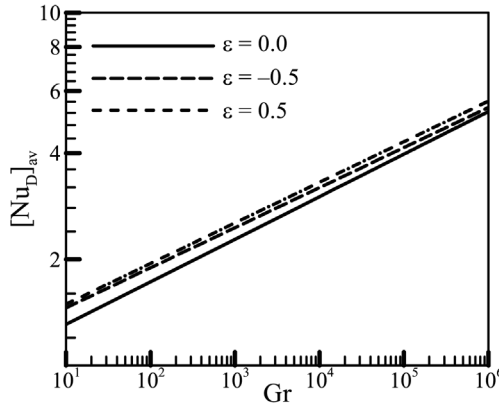

Figure 10.
Average Nusselt number as a function of Grashof number at different ε

($L/D = 2.0$). Effect of L/D ratio on heat transfer is also presented. Eccentricity greatly affects the flow and thermal fields as well as the heat transfer distribution. Eccentric positions of the cylinder show higher heat transfer rate than concentric position. At all values of ε, circulatory zone with one core is observed near the upper part of the cylinder. Again for $\varepsilon = 0.0$, a critical range of Grashof number is identified below which heat transfer is higher for lower L/D ratio and above which heat transfer is lower for lower L/D ratio.

Notes

1. 306-106 Seagram Drive, Waterloo, Ontario, Canada, N2L3B8, Email: shtasnim@yahoo.ca

2. Department of Mechanical Engineering, University of Waterloo, Waterloo, Ontario, Email: smahmud@engmail.uwaterloo.ca

3. Department of Mechanical Engineering, University of Alberta, Edmonton, Alberta, Canada, T6G2G8, Email: pdas@ualberta.ca

References

Cesini, G., Paroncini, M., Cortella, G. and Manzan, M. (1999), "Natural convection from a horizontal cylinder in a rectangular cavity", *Int. J. Heat Mass Transfer*, Vol. 42, pp. 1801-11.

Farouk, B. and Guceri, S.I. (1981), "Natural convection from horizontal cylinder – laminar regime", *ASME J. Heat Transfer*, Vol. 103, pp. 522-6.

Ferziger, J. and Peric, M. (1996), *Computational Methods for Fluid Dynamics*, Springer Verlag, Berlin, Hedelberg.

Kuhen, T.H. and Goldstein, R.J. (1976), "An experimental and theoretical study of natural convection in the annulus between horizontal concentric cylinders", *J. Fluid Mechanics*, Vol. 74, pp. 695-719.

Kuhen, T.H. and Goldstein, R.J. (1978), "An experimental study of natural convection heat transfer in concentric and eccentric horizontal cylindrical annuli", *J. Heat Transfer*, Vol. 100, pp. 635-40.

Patankar, S.V. (1980), *Numerical Heat Transfer and Fluid Flow*, McGraw-Hill, New York.

Prusa, J. and Yao, L.S. (1983), "Natural convection heat transfer between eccentric horizontal cylinders", *ASME, J. of Heat Transfer*, Vol. 105, pp. 108-16.

Tasnim, S.H. and Mahmud, S. (1999), "Flow and thermal field behavior around an isothermal square cylinder in a large confined enclosure", 3rd Int. Conference on Fluid Mech. and Heat Transfer, ICFMHT-99, Dhaka, Bangladesh, pp. 212–217.